

Tissue size controls patterns of cell proliferation and migration in freely-expanding epithelia

Matthew A. Heinrich^a, Julienne M. LaChance^a, Tom J. Zajdel^a, Ricard Alert^{b,c}, Andrej Košmrlj^{a,d}, and Daniel J. Cohen^{a,1}

^aDepartment of Mechanical and Aerospace Engineering, Princeton University, Princeton, NJ 08544

^bLewis-Sigler Institute for Integrative Genomics, Princeton University, Princeton, New Jersey 08544, USA

^cPrinceton Center for Theoretical Science, Princeton University, Princeton, New Jersey 08544, USA

^dPrinceton Institute for the Science and Technology of Materials (PRISM), Princeton University, Princeton, New Jersey 08544, USA

In the last decade, key advances in our understanding of collective cell migration and tissue growth have been made by studying the expansion of epithelial monolayers in vitro. However, most studies have focused on monolayers of sub-millimetric sizes, and how cell proliferation and migration are coordinated on larger scales remains poorly known. To fill this gap, we measured cell velocity, cell density, and cell-cycle state over 2 days in millimeter-scale freely-expanding monolayers. We find that tissues of different initial sizes exhibit very different spatiotemporal patterns of cell proliferation and collective cell migration in their internal regions. Specifically, within several cell cycles, the core of large tissues becomes very dense, almost quiescent, and ceases cell-cycle progression. In contrast, the core of smaller tissues develops a local minimum of cell density as well as a tissue-spanning vortex. These different dynamics are determined not by the current but by the initial tissue size, indicating that the state of the tissue depends on its history. Despite these marked differences at the internal regions, the edge zone of both large and small tissues displays rapid cell-cycle progression and radially-oriented migration with a steady velocity independent of tissue size. As a result, the overall area expansion rate is dictated by the perimeter-to-area ratio of the tissue. Our findings suggest that cell proliferation and migration are regulated in a collective manner that decouples the internal and edge regions of the tissue, which leads to size- and history-dependent internal patterns in expanding epithelia.

tissue growth | cell cycle | collective migration | epithelia

Correspondence: danielcohen@princeton.edu

Introduction

Writing in 1859, physiologist Rudolf Virchow presented the concept of the ‘Zellenstaat’ or ‘Cell State’, describing tissues as “a society of cells, a tiny well-ordered state” (1). This social framework motivated Abercrombie and Heaysman’s 1954 work on cellular behavior that elucidated how encounters between cells can regulate locomotion and proliferation via contact inhibition (2). Since then, concerted interdisciplinary effort has been brought to bear on understanding how cell-cell interactions give rise to the complex collective behaviors driving so many crucial biological processes. One of the most foundational collective behaviors is collective cell migration—the directed, coordinated motion of cellular ensembles that enables phenomena such as gastrulation, wound healing, and tumor invasion (3). Given this importance, considerable effort spanning biology, engineering, and physics has been directed towards understanding how local

cellular interactions can give rise to globally coordinated motions (4, 5).

Due to the complexity of collective behaviors, much effort has gone towards reductionist assays that restrict degrees of freedom and ensemble size to simplify analysis and interpretation. One powerful approach is to confine a tissue within predefined boundaries using micropatterning to create adhesive and non-adhesive regions (6–11). Such confinement mimics certain in vivo contexts such as constrained tumors as well as aspects of compartmentalization during morphogenesis (12). Alternately, many studies have explored the expansion of tissues that initially grow into confluence within confinement but are later allowed to migrate into free space upon removal of a barrier. A popular assay of this type relies on rectangular strips of tissue that are allowed to expand in one or both directions (13–21), where averaging along the length of the strip can reveal coordinated population-level behaviors such as complex migration patterns, non-uniform traction force fields, and traveling mechanical waves. Isotropic expansion has also been studied in the context of micro-scale (< 500 μm diameter) circular tissues using the barrier stencil technique (22) as well as photoswitchable substrates (23), revealing behaviors associated with initial expansion of a tissue. In contrast to such confinement assays, other work has focused on freely-expanding tissues of uncontrolled initial size and shape, which grow from either single cells (24) or cell-containing droplets (9, 25, 26). Still more work has explored approaches to induce directional migration, from geometric cues to applied electric fields (27, 28). Together, these assays have begun to uncover general principles underlying collective cell migration.

Studies of collective cell migration are most often performed using epithelial tissues due to their fundamental role in multicellular organisms and strong cell-cell adhesion, which in turn gives rise to elegant, cohesive motion. Moreover, given that epithelia naturally form surfaces in vivo, studying epithelial layers in vitro has a physiological basis that can inform our understanding of processes such as healing (13), envelopment (29), and boundary formation (30). These features have made epithelia both the gold standard in collective cell migration studies, and one of the most well-studied models for biological collective behaviors.

Despite our deep reductionist understanding of cellular-scale aspects of collective migration in epithelia, we lack a basic systems-level understanding of how tissue size and shape af-

fect long-term epithelial growth. Answering such basic questions has broad utility across cell biology, biophysics, and tissue engineering, where prediction of growth and form can be advantageous. Hitherto, most studies have restricted tissue growth and expansion to the micro-scale (< 500 microns), short durations (< 24 hrs), and confined geometries. Noting these limitations is important because differences in scale, time, and boundary conditions can lead to unexpected emergent complexity, as we show here.

As a demonstration, we began by asking “How does tissue size affect epithelial spreading and growth?” To address this seemingly basic question, we leveraged benchtop tissue patterning (13, 31) to rapidly generate arrays of precisely patterned, unconfined epithelia at the macro-scale (>1 mm in diameter), and performed long-term time-lapse imaging (up to 48 hrs). We investigated the role of tissue size and shape on boundary motion, and we then tracked every cell in the tissues to relate the overall expansion kinetics to cell migration speed, cell density, and cell-cycle dynamics. In addition to yielding a new understanding of the role of epithelial size and shape in overall growth, our studies reveal an unexpected, size-dependent process that can induce large-scale vortices in freely expanding epithelia. Together, these data comprise the first comprehensive study of macro-scale, long-term epithelial expansion, and our findings demonstrate the importance of exploring collective cell migration across a wider range of contexts, scales, and constraints.

Results

Effects of size and shape on expansion of millimeter-scale epithelia. We began by characterizing how the initial tissue area affects areal expansion and cell growth. An important length scale relevant to any migrating population is the velocity-velocity correlation length, which is $\ell_v \sim 200 \mu\text{m}$ in MDCK epithelia (15). Epithelial tissues with characteristic sizes below the correlation length have been shown to exhibit collective cell behaviors different from tissues larger than the correlation length (6, 27). In addition to these size-dependent effects at the sub-millimetric scale, growing epithelia have been shown to jam when the colony reaches millimetric scales (24), indicating that tissue size may play an important role in tissue behavior at these larger scales.

To conclusively address how tissue size influences long-term growth, we measured the expansion of confluent circular tissues with the same cell density but different initial diameters of 1.7 mm and 3.4 mm (a 4X difference in area, with tissues hereafter referred to as either “small” or “large”). We patterned the tissues by culturing cells in circular silicone stencils of controlled size for ~ 18 hrs (13, 31), whereupon stencils were removed and tissues were allowed to freely expand for 46 h (Fig. 1A, Movie S1), while images were collected at 20 minute intervals using automated microscopy (see SI Supplementary Methods). Our cell seeding conditions and incubation period were deliberately tuned to ensure that the stencils did not induce contact inhibition or jamming prior to stencil removal. Upon stencil removal, tissues expanded while maintaining their overall circular shape throughout the

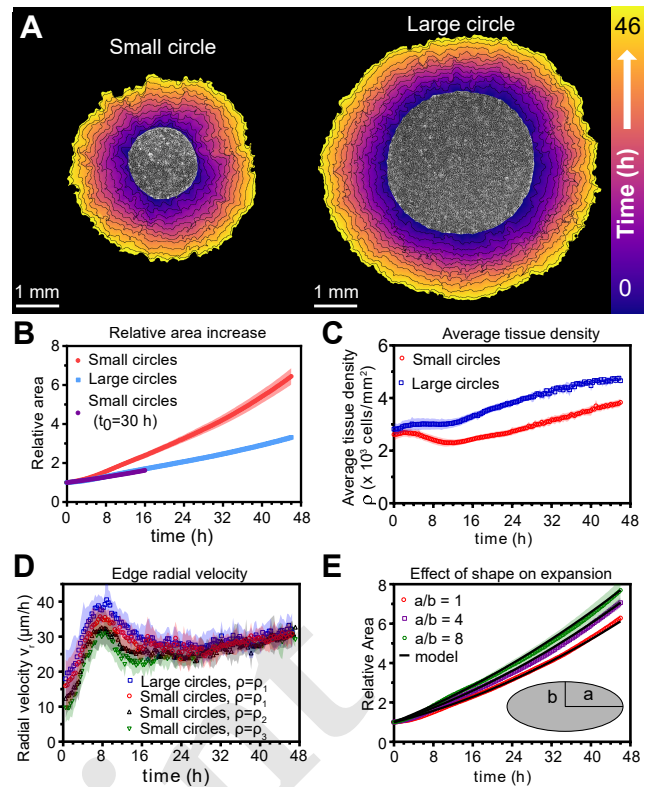


Fig. 1. Expansion dynamics of millimeter-size cell monolayers. (A) Footprint throughout 46 h growth period of representative small (left) and large (right) circular tissues, with the tissue outlines drawn at 4 h increments. Initial diameters were 1.7 mm and 3.4 mm. (B) Small circles exhibit faster relative area, $A(t)/A_0$, increase than large circles, where A_0 and $A(t)$ are the areas of tissues at the beginning of the experiment and at time t , respectively. Purple points show the relative area increase, $A(t+t_0)/A(t_0)$, of small tissues from the time $t_0 = 30$ h when they reached the size of the large circles. (C) Average tissue density $N(t)/A(t)$ has non-monotonic evolution in small tissues but monotonically increases in large tissues. (D) Edge radial velocity is largely independent of initial tissue size and cell density. We grouped initial cell densities as $\rho_1 = [2350, 3050]$ cells/mm², $\rho_2 = [1650, 2350]$ cells/mm², and $\rho_3 = [1300, 1650]$ cells/mm². (E) Assuming a constant migration speed v_n in direction normal to the edge, we can predict the area expansion dynamics of elliptical tissues with different aspect ratios. Fitting the model to our data for all tissues gives $v_n = 29.5 \mu\text{m/h}$. In B, data are from $n=16$ tissues across 5 independent experiments (small and large circles). In C, $n=11$ across 4 experiments for small circles, and $n=9$ across 3 experiments for large circles. In D, $n=16$ across 5 independent experiments for small and large circles, $\rho = \rho_1$; $n=13$ across 3 experiments for small circles, $\rho = \rho_2$; and $n=11$ across 3 experiments for small circles, $\rho = \rho_3$. In E, $n=4$ across 2 experiments for $a/b=1$ and $a/b=4$, and $n=5$ across 2 experiments for $a/b=8$. Shaded regions correspond to standard deviations.

2-day experiment. To place our results in the context of prior studies, we worked with the widely-used MDCK epithelial cell line, in our case stably expressing the 2-color FUCCI cell cycle marker to allow us to relate dynamics to proliferation (20, 26, 32, 33). Unless otherwise noted, cell density at stencil removal was ~ 2700 cells/mm², a value consistent with active and growing confluent MDCK epithelia (20, 33). First, we measured relative areal increase (Fig. 1B) and relative cell number increase (SI Appendix, Fig. S1) of small and large tissues. By 46 h, small and large tissues had increased in area by 6.4X and 3.3X, respectively, while cell number increased by 9.2X and 5.5X, respectively (Fig. S1). Since proliferation outpaces area expansion in long-term growth, average tissue density increased by the end of the experiment.

The evolution of average tissue density was more complex, however, as small tissues experienced a transient density decrease while large tissues exhibited a monotonic increase in cell density (Fig. 1C). Accordingly, at any given time (after stencil removal), large tissues had a higher density than small tissues. Non-monotonic density evolution has been observed in thin epithelial strips (13) and likely arises from competition between migration and proliferation dynamics, which we discuss later. Given that the MDCK cell cycle is known to last approximately 16 hrs (20, 33), our observation of a transient density decrease in small tissues demonstrates that migration plays a stronger role than cell division at early stages of tissue expansion.

We then related area expansion to the kinematics of the tissue edge. To quantify edge motion, we calculated the average radial velocity of the tissue boundary, $v_r(t)$, at 1 hr intervals over 46 hrs (SI Supplementary Methods). We found that v_r is independent of both tissue size and a wide range of initial cell densities, in all cases reaching $\sim 30 \mu\text{m/h}$ after ~ 16 h (Fig. 1D). Before that, v_r ramps up during the first 8 h after stencil removal, and, notably, overshoots its long-time value by almost 30%. We hypothesize that the overshoot is due to the formation of fast multicellular finger-like protrusions that emerge at the tissue edge in the early stages of expansion and then diminish (Movie S2). This hypothesis is supported by a recent model showing that edge acceleration (as observed during the first 8 h in Fig. 1D) leads to finger formation (34). The fact that initial density does not have a more significant effect on the edge speed further supports our hypothesis and suggests that, even at early stages, epithelial expansion is primarily driven by cell migration at the tissue edge rather than density-dependent decompression and cell spreading. Additionally, the observation that v_r is independent of tissue size ought to explain why small circular tissues have faster area expansions than large circular tissues.

To further formalize our understanding of epithelial expansion, we hypothesized that the relation between tissue size and areal increase could be attributed primarily to the perimeter-to-area ratio. Assuming a constant edge velocity v_n normal to the tissue boundary, the tissue area increases as $dA = P v_n dt$, where P is the perimeter of tissue and dt is a small time interval. Thus, the relative area increase $dA/A = (P/A) v_n dt$ scales as the perimeter-to-area ratio. For circular tissues $P/A \propto 1/R$ is inversely proportional to the radius R and thus the relative area increases faster for smaller tissues (Fig. 1B). In order to verify that the perimeter-to-area ratio is proportional to the relative area increase, we analyzed tissue expansion for a series of tissue shapes (circles and ellipses) with the same area and tissue density but different perimeter (Movie S3). While edge curvature was shown to influence closure of micro-scale gaps in epithelial monolayers (35, 36), the influence of shape on the overall outgrowth of macroscopic tissues is not well characterized. Here, we see that increasing the perimeter-to-area ratio of a tissue by increasing its aspect ratio indeed increases the areal expansion rate (Fig. 1E). For these elliptical tissues, our edge-driven expansion model predicts $A(t)/A(0) = (a + v_n t)(b + v_n t)/(ab)$,

where a and b are the initial major and minor axes of the ellipse. Using the same edge speed $v_n \simeq 29.5 \mu\text{m/h}$ for all tissues, this prediction fits all of our data well (Fig. 1E). Together, our findings demonstrate that epithelial shape and size determine area expansion dynamics via the perimeter-to-area ratio. This relationship results from the fact that tissues exhibit a constant, size-independent, migration-driven edge speed normal to tissue boundary.

Spatiotemporal dynamics of migration speed and radial velocity. Having demonstrated the role of the boundary in the expansion of large-scale epithelia, we next explored how that behavior emerges from cellular dynamics within the bulk of the epithelium. We first sought to relate tissue areal expansion rate to internal collective cell migration dynamics. Here, we used Particle-Image-Velocimetry (PIV, See SI Appendix) to obtain flow fields describing cell migration within freely expanding epithelia (13, 15, 28, 37, 38). Averaging the flow fields over the angular direction and over 16 tissues (SI Supplementary Methods), we constructed kymographs to describe the spatiotemporal flow patterns of the tissue (18, 19) (see representative kymographs in SI Appendix, Fig. S2). The speed kymographs reveal the existence of an edge region of fast cell motion (Fig. 2A). In small tissues, we observe a motile interior region up to 1 mm wide that is separated from the outer region by a transition zone of lower speed and is just beginning to become quiescent by 46 h (Fig. 2C). In large tissues, on the other hand, the interior region becomes almost completely quiescent after ~ 28 h (Fig. 2B,C).

We then focused on just the center zone, which we define as having a radius $\sim 200 \mu\text{m}$, roughly corresponding to the velocity correlation length ℓ_v . From 20 to 40 h, cell speed decreases steadily in the center of large tissues but remains high for small tissues (Fig. 2A, B top). After about 30 h cell speed also decreases for small tissues. Decrease in cell speed in an epithelium is often attributed to either contact inhibition of locomotion (CIL) or cell jamming (39–42), which we will discuss later.

We then turned to the outer zone, which we defined as extending $\sim 200 \mu\text{m}$ inward from the boundary. Notably, cell speeds in this region are insensitive to the changes observed in the tissue center, regardless of tissue size (Fig. 2A and B bottom). Both small and large tissues exhibit a high, constant speed at the edge region (Fig. 2B bottom), consistent with the constant radial edge velocity reported in Fig. 1D. However, the peripheral speed evolution (Fig. 2B, bottom) does not exhibit the overshoot seen in Fig. 1D, suggesting that the non-monotonous evolution of the edge radial velocity is due to boundary effects rather than to the cell flows in the extended peripheral region (PIV windows span multiple cells and smooth high-wavevector components of the flow field). Hence, our peripheral speed data are consistent with our hypothesis that the edge velocity overshoot is due to formation of fingers at the tissue boundary. The decay of cell speed from the tissue edge demonstrates the ultra-conserved boundary behavior, with the profiles for both small and large tissues matching almost exactly for the outer $\sim 500 \mu\text{m}$ of the tissue (Fig. 2C top). Further into the tissue interior the speed pro-

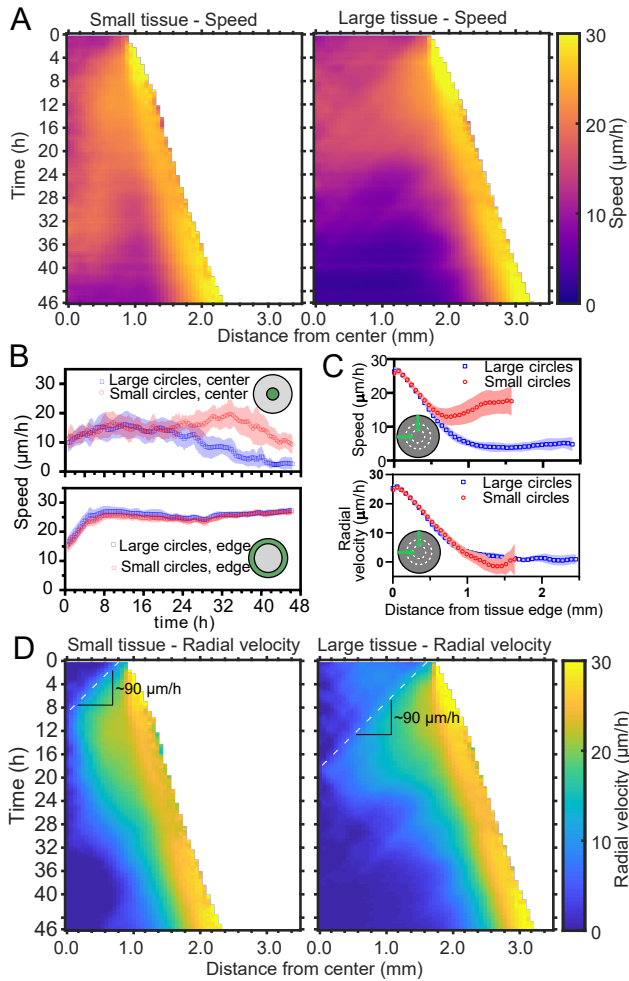


Fig. 2. Speed and radial velocity in inner and outer tissue zones. (A) Average kymographs of speed throughout expansion for small (left) and large (right) tissues (see representative kymographs and heatmaps in SI Appendix, Fig. S2). Note that the outer boundary region of the averaged kymographs is somewhat stretched due to variation in tissue expansion speeds and edge roughness causing misalignment between boundaries of different tissues. (B) Evolution of the average speed of center (top) and boundary (bottom) zones. These zones were defined as regions extending $\sim 200 \mu\text{m}$ from the tissue center and tissue edge, respectively. The edge zone speed is independent of tissue size, consistent with the size-independent edge radial velocity shown in Fig. 1D. The center zone speed begins to decrease ~ 12 h sooner in large tissues than in small tissues, as the central zone of the small tissues has particularly high speed from 18-36 h. (C) Profiles of speed (top) and radial velocity (bottom) at 36 h, from the edge of the tissue inwards. Arrows indicate that the tissues are indexed from the edge of the tissue inwards. (D) Kymographs of radial velocity v_r reveal progressive outward mobilization of the tissue at early times (dashed lines) and low radial velocity region in small and large tissues at late times.

file of the small tissue diverges from the large tissue, where small tissues have the higher-speed central region, while in large tissues the speed continues to decay toward very low values.

To separately consider cell motion that contributes to tissue spreading, we also computed the radial component of the velocity field, v_r . In contrast to overall speed, radial velocity profiles for both large and small tissues match almost identically (Fig. 2C bottom). Here, the outward flow is conserved across tissue size even when overall speed is much different. Kymographs of v_r further reveal the dynamics of this outward flow. We find that rapid increase in radial velocity

propagates inward toward the center of the tissue after stencil removal at $\sim 90 \mu\text{m/h}$ (Fig. 2D dashed lines), which is approximately 3X faster than the speed of the tissue edge expansion, consistent with previously described waves of strain rate in cell monolayers (18). Strikingly, soon after the wave of rapid radial velocity increase reaches the center of the tissues, it then quickly retreats, leaving a region of low radial velocity that grows in extent in the center of both small and large tissues. In large tissues this is mirroring the reduction in cell speed (Fig. 2A), but in small tissues the speed in the center region remained high, suggesting a large structure with high tangential velocity. We investigate this type of motion in the next section.

Emergence of large-scale vortices. The propagation of low radial velocity out from the center of small tissues coincides with the formation and expansion of a millimeter-scale, persistent vortex (Fig. 3A, Movie S4 for representative vortex). While smaller and more transient vortices are observed in large tissues (Movie S5), only small tissues exhibit tissue-spanning, fast, and persistent vortices. Vortices near the tissue centroids are the most common, but we also observe smaller, off-center vortices and co-rotating vortex pairs (see SI Appendix, Fig. S5).

To visualize the form and scale of the vortices, we tracked individual cell motion and colored cell trajectories according to their orientation (43) (see Fig. 3A and SI Supplementary Methods). We plotted 10 h trajectories during the 0-20 h and 20-40 h time-periods separately; the vortex was most apparent during the 20-40 h time-period in small tissues (Fig. 3A, left) and 0-20 h time-period in large tissues (Fig. 3A, right; see SI Appendix, Fig. S3 for all time-periods). In small tissues, cell trajectories are primarily radial in the boundary zone, but mainly tangential in the central zone (Fig. 3A left). Accordingly, cell trajectories that start further away from the tissue center lead to larger radial displacements (red markers in Fig. 3B), while trajectories that start near the center lead to larger tangential displacements (blue markers in Fig. 3B). The tangential displacement profile most clearly reveals the presence of the vortex, with $\sim 350 \mu\text{m}$ tangential displacement throughout the central $750 \mu\text{m}$ of the tissue. At the outer zone, tangential displacements drop to $\sim 0 \mu\text{m}$. In contrast, radial displacement (red markers in Fig. 3B) increases roughly linearly from the center to the outer edge of the tissue, with no sharp change when moving from the central to the outer region. The fact that radial displacements are largely insensitive to the vortical flows explains why the presence of a vortex has no noticeable impact on the overall expansion of the tissue. Together, the radial and tangential displacements of the tissue reveal a spiraling vortical flow that combines tangential shear with radial expansion.

To further characterize the vortices, we obtained the vorticity field $\omega(\mathbf{r}, t) = \nabla \times \mathbf{v}(\mathbf{r}, t)$. Before averaging over tissues, we took the dominant direction of rotation of each tissue to correspond to positive vorticity. This direction was counterclockwise in 51.5% of tissues and clockwise in 49.5% of tissues, with a sample size of 68. With this convention, the vortex core always has positive vorticity. Accordingly, the outer re-

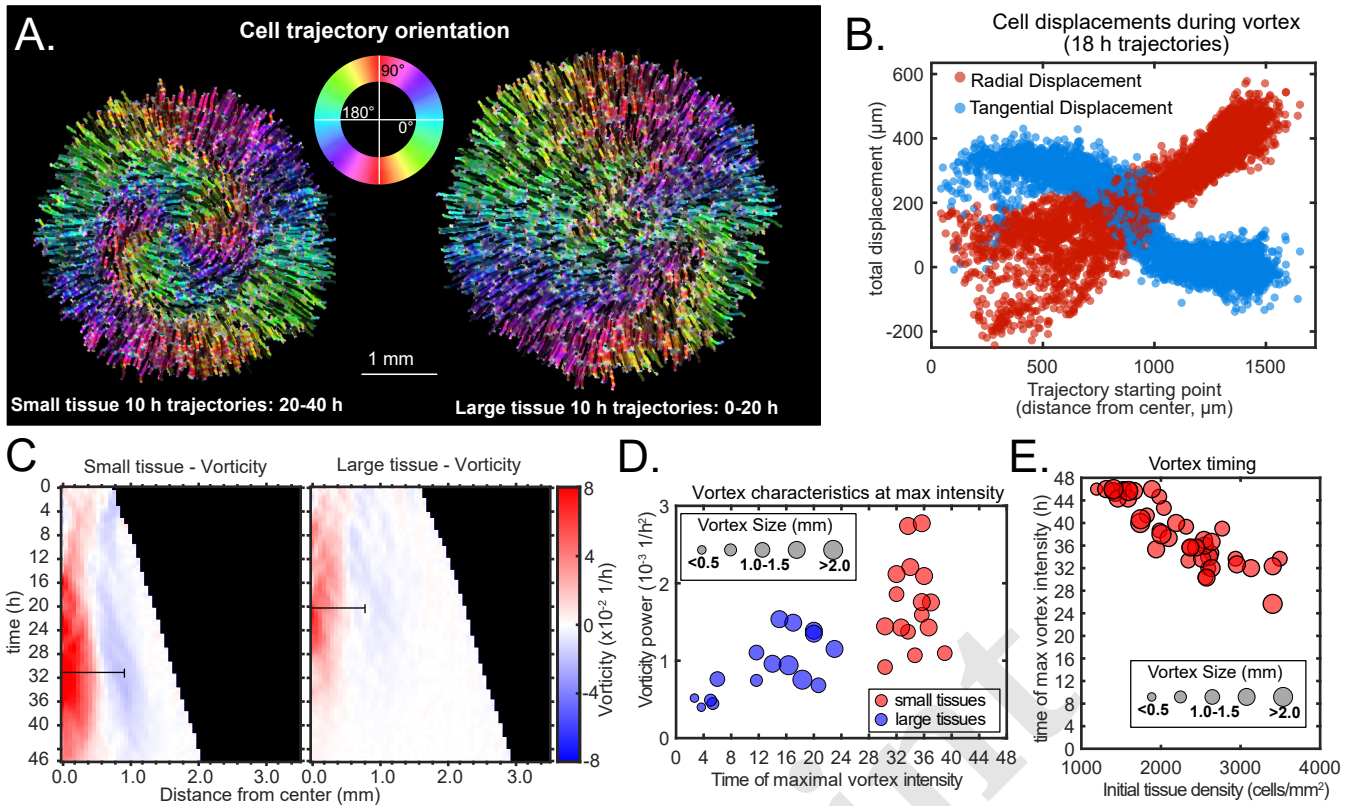


Fig. 3. Vortex formation in expanding tissues. (A) Vortical flows seen from 10 h traces of cell trajectories in small (left) and large (right) tissues, which we show during the 20–40 h and 0–20 h time periods, respectively. We color each trajectory according to its local orientation. Scale bar. (B) Radial and tangential displacements of 18 h cell trajectories for a representative small tissue as a function of the initial radial position of each cell trajectory. Trajectories were selected from the vortex-dominated period of 24–42 h (SI Supplementary Methods). Radial displacements exhibit no sharp transition between the central vortical region and the outer region of radial expansion. In contrast, tangential displacements are high throughout the central vortical region and drop at the outer region. (C) Average kymographs of vorticity show that the vortex in small tissues appears in the center and expands to >1 mm ($n = 16$), while vorticity in large tissues is generally weaker except during the early stages of tissue expansion ($n = 16$). The black bars indicate a characteristic vortex size. (D) Characteristic size (marker size), time (horizontal axis), and intensity (vertical axis) of each tissue's maximal vortex intensity. (E) For small tissues, the time of maximal vortex intensity correlates negatively with the initial cell density.

gion of the vortex exhibits negative vorticity (Fig. 3C), which corresponds to the counter-rotation that occurs when the central vortical flow transitions to the outer radial flow (Fig. 3A, left). We define a characteristic vortex radius as the radial position of the center of the negative-vorticity region, which is ~ 1 mm at 36 h in small tissues (Fig. 3C, black bars).

To better analyze vortex dynamics across different tissues with varying vortex positioning, and to more quantitatively capture the onset and strength of vortices, we calculated the enstrophy spectrum $\mathcal{E}(q, t) = |\tilde{\omega}(\mathbf{q}, t)|^2$, where $\tilde{\omega}(\mathbf{q}, t)$ are the spatial Fourier components of the vorticity field $\omega(\mathbf{r}, t)$ (44). The enstrophy spectrum is the the power spectral density of the vorticity field as a function of the wave-vector modulus q , and therefore provides a measure of the vortex intensity at a length scale $2\pi/q$. The kymographs of the enstrophy spectrum show that most of the vortex's intensity is found at a characteristic length scale of ~ 1 mm (SI Appendix, Fig. S4). For each tissue we characterized the maximal vortex strength by the maximum value of $\mathcal{E}(q, t)$ as well as its associated wavelength $2\pi/q$ and time of occurrence. We represented these three quantities on a scatter plot, which shows that vortices in small tissues have generally higher intensity than in large tissues (Fig. 3D). Vortices in small tissues are also larger relative to tissue size, since the absolute size of vortices in

small and large tissues is similar (Fig. 3D). Furthermore, vortices become maximally strong several hours later in small tissues than in large tissues (Fig. 3D). We hypothesized that this difference is due to large tissues featuring a faster density increase than small tissues (Fig. 1C). To test this hypothesis, we varied the initial cell density of small tissues and observed that the initial cell density correlates negatively with the time of maximal vortex strength (Fig. 3E, SI Appendix, Fig. S4). These results prompted us to further examine the spatiotemporal evolution of the cell density field.

Spatiotemporal dynamics of cell density. Given that cell density appears to affect vortex formation and is known to control contact inhibition of locomotion and proliferation, we further explored the spatiotemporal evolution of cell density. Constructing average kymographs in the same way as for speed, radial velocity, and vorticity, we observe that the vortex region in the center of small tissues is accompanied by an unexpected local density minimum (Fig. 4A). As seen in representative snapshots of small and large tissues (SI Appendix, Fig. S5A–D), low-density regions typically co-localize with large-scale vortices, even when they are located away from the center of the tissue. However, given that vortices in large tissues are often off-centered, the low-density region does not

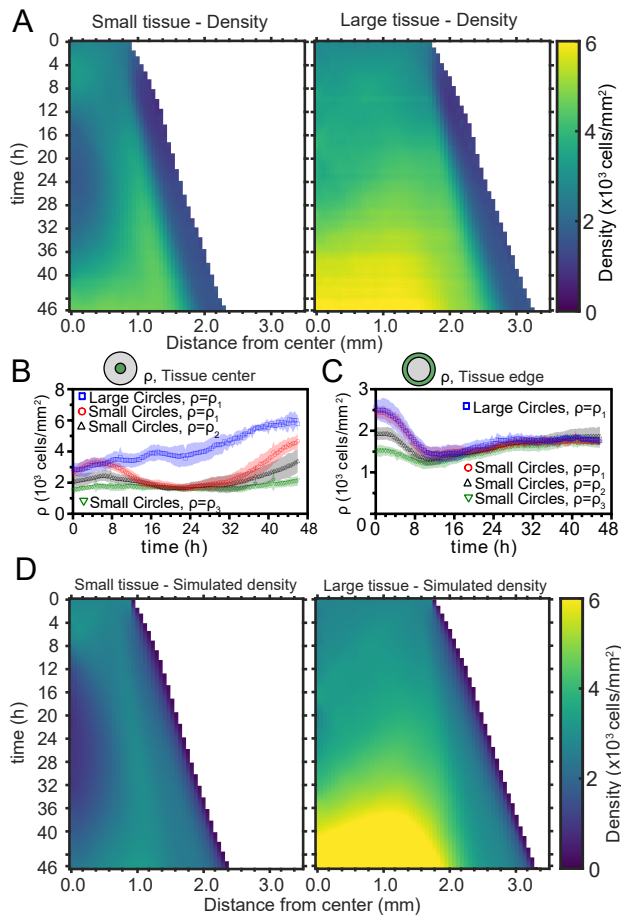


Fig. 4. Spatiotemporal dynamics of cell density during epithelial expansion (A) Averaged kymographs of cell density for small (left, $n=11$) and large (right, $n=9$) tissues. The high speed, high directional boundary zone from Fig. 2 is seen to be at the lower limit of confluence, ~ 1000 cells/ mm^2 , throughout the expansion. Small tissues develop a central low-density region that persist more than 20 h. (B) Cell density at the center of large tissues increases gradually, while cell density at the center of small tissues has non-monotonic evolution. (C) For different initial tissue sizes and densities, the evolution of the cell density at the boundary zone converges to similar values at about 12 h, which coincides with the end of the overshoot of edge radial velocity in Fig. 1D. Center and boundary zones are defined as in Fig. 2B. We grouped initial cell densities as $\rho_1 = [2350, 3050]$ cells/ mm^2 , $\rho_2 = [1650, 2350]$ cells/ mm^2 , and $\rho_3 < 1650$ cells/ mm^2 . (D) Simulated evolution of cell densities obtained from the numerical solution of the continuity equation using the measured radial velocity $v_r(r, t)$ and a uniform and constant cell proliferation rate corresponding to a 16 h cell doubling time. In (B,C) the initial cell density ranges ρ_1 , ρ_2 , and ρ_3 are the same as in Fig. 1D.

appear in their average kymograph of cell density.

To further characterize the spatiotemporal features of the density field, we tracked the density evolution of the center and boundary zones across tissues with different starting densities and sizes, grouping initial densities into 3 ranges as before (Fig. 4B and C). As expected, the cell density at the center of large tissues increases throughout the experiment. In contrast the cell density at the center of small tissues initially increases, then undergoes a transient density decrease, and finally increases again. Notably, the cell density at the center of small tissues of different initial cell densities reach a common minimum during the 16-32 h time period, which includes the time of initiation of the vortex. At the boundary zone, the long-time evolution of the cell density is independent of initial tissue size and density (Fig. 4C). This common

long-time evolution is reached at about 12 hours (Fig. 4C), which coincides with the time at which the edge radial velocity stabilizes upon the overshoot (Fig. 1D).

To understand the unexpected transient density decrease at the center of small tissues, we sought to explain it as the result of combined advective transport based on the measured radial flow fields $\mathbf{v}_r(\mathbf{r}, t)$ and homogeneous cell proliferation at a rate $k(\mathbf{r}, t) = k_0$ throughout the tissue. To test this hypothesis, we solved the continuity equation for the cell density field $\rho(\mathbf{r}, t)$,

$$\frac{\partial \rho}{\partial t} = -\nabla \cdot (\rho \mathbf{v}_r) + k_0 \rho, \quad (1)$$

using the average radial velocity profiles $v_r(r, t)$ measured by PIV (Fig. 2D), and a proliferation rate $k_0 = 1.04 \text{ h}^{-1}$, which corresponds to a cell doubling time of 16 h (SI Appendix, Supplementary Materials and Methods). This minimal model recapitulates the major features of the evolving density profiles for both small and large tissues (compare Fig. 4D with Fig. 4A). Therefore, the unexpected formation of a central low-density region results from the combination of outward tissue flow and simple exponential growth of the colony. However, further research is required to determine the biophysical origin of the non-monotonic density evolution. Moreover, assuming a density-independent proliferation rate, our model predicts a cell density in the center of large tissues higher than the one measured at the end of the experiment, and it does not quantitatively reproduce the cell density profiles at the edge regions. These discrepancies suggest that more complex cell proliferation behavior is required to fully recapitulate the density dynamics in expanding cell monolayers.

Spatiotemporal dynamics of cell cycle. Next, we analyzed the spatiotemporal dynamics of cell-cycle state within expanding millimetric tissues. Our cells stably express the FUCCI markers, meaning that cells in the G0-G1-S phase of the cell cycle (referred to here as G1) fluoresce in red (shown as magenta), and cells in the S-G2-M phase of the cell cycle (referred to here as G2) fluoresce in green (32). Additionally, immediately-post-mitotic cells do not fluoresce and appear dark. The dominant presence of green cells at the time of stencil removal confirms that cells are actively cycling at the onset of tissue expansion (SI Appendix, Fig. S6). By the end of the experiment, the outer zone of both large and small tissues is primarily populated by G2 cells (Fig. 5A, Movie S6, green) and post-mitotic cells (Fig. 5A inset). In contrast, the inner zone of large tissues is almost entirely comprised of G1 cells (Fig. 5A, Movie S6, magenta), while the central zone of small tissues maintained more well-mixed cell-cycle states. A G2-dominated outer zone and G1-dominated inner zone had also been seen in 3D cell aggregates spreading onto a surface, indicating that this feature is a general motif in multicellular spreading and growth (26).

To quantitatively investigate cell-cycle spatiotemporal dynamics, we obtained the local fractions of G1, G2, and post-mitotic cells by comparing the fluorescence intensities at each nucleus location (SI Materials and Methods).

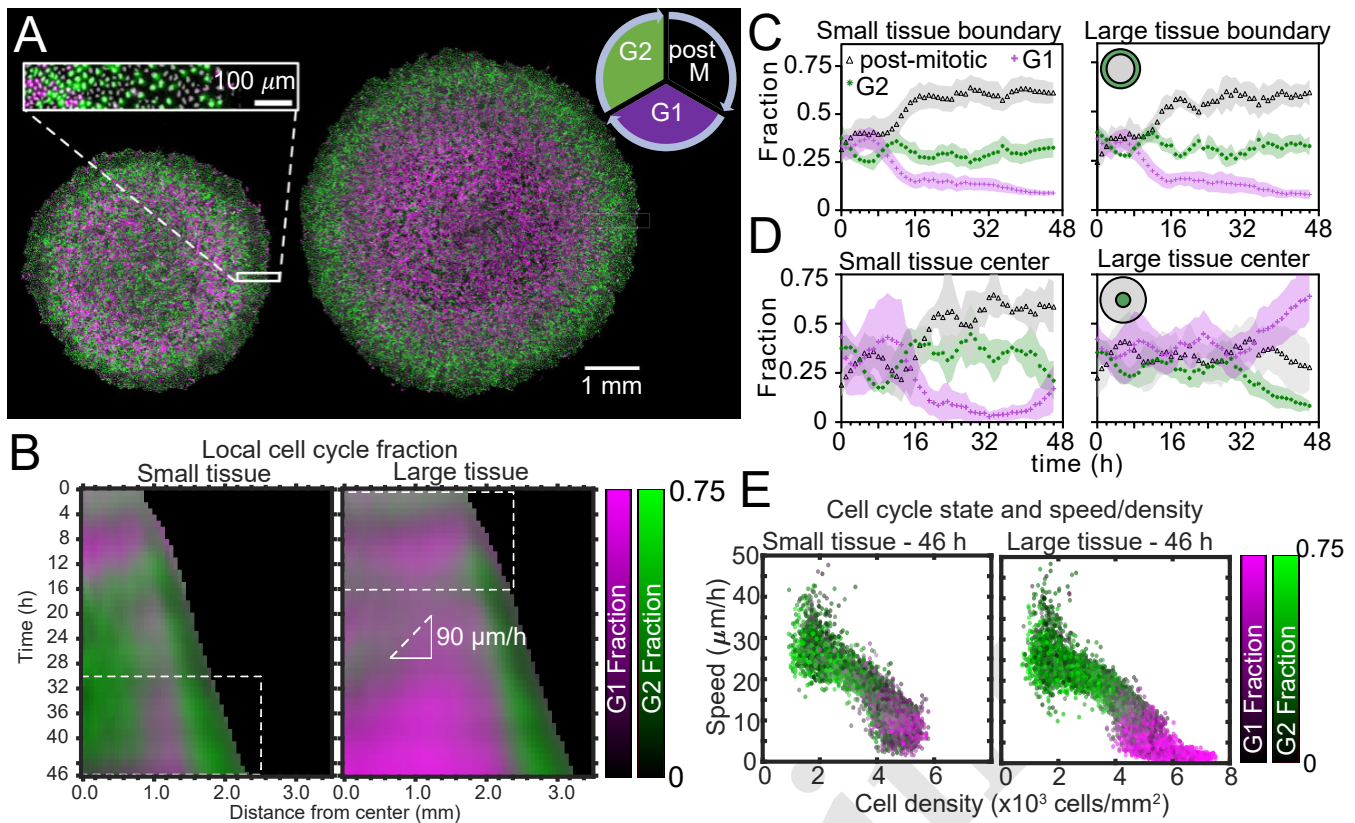


Fig. 5. Coordinated spatiotemporal cell-cycle dynamics. Transition from the G1 (magenta) to the G2 (green) phase of the cell cycle corresponds to DNA replication (during S phase). Subsequently, a cell proceeds to mitosis (M phase, dark), and eventually back to the G1 phase upon cell division. (A) Fluorescence images of the Fucci marker of cell-cycle state at the end of the experiment (46 h) of representative small and large tissues overlaid with nuclei positions (gray). At the end of the experiment, the center of large tissues consists mainly of cells in the G1 phase while the center of small tissues is composed of cells that are in different stages of cell-cycle. The boundary zone of both tissues has more cells in the G2 than in the G1 phase, along with a substantial proportion of dark cells (inset). Scale bars 1 mm. (B) Average kymographs (small, n=5; large, n=11) of cell-cycle-state fraction. In large tissues, a front of G1-dominated (magenta) cell-cycle state begins in the transition zone between the central and boundary regions and propagates toward the center at $\sim 90 \mu\text{m/h}$. While the size of small tissues from 30 to 46 h matches that of large tissues from 0 to 16 h (dashed boxes), cell-cycle states are clearly distinct. (C) The fraction of cell-cycle states in the boundary zone of small and large tissues evolves nearly identically and is dominated by G2 and dark cells, indicating rapid cycling. (D) The cell-cycle state in the central zone of small tissues proceeds similarly to their edge, whereas the central zone of large tissues has well-mixed cell-cycle states until the onset of contact inhibition of proliferation at ~ 30 h. Center and boundary zones are defined as in Fig. 2. (E) Scatter plot of density and speed, with color indicating the fraction of cells at G1 and G2, corresponding to each PIV pixel of the final timepoint of a representative small (left) and large (right) tissue. The small tissue does not contain the slow, high-density, G1-dominated population that is present in the large tissue (magenta dots on the bottom right). In the large tissue, a relatively sharp transition from G2-dominated fast cells to G1-dominated slow cells occurs over a small increase in cell density.

We constructed average kymographs of the cell-cycle-state fractions and overlaid the kymographs for the G1 and G2 states (Fig. 5B). This representation revealed that the contact-inhibited state (magenta) that dominates the center of large tissues from 30 h onward does not originate in, or propagate out from, the dense core of the tissue. Instead, a front of contact inhibition of proliferation (CIP) seems to initiate between the central and edge zones at ~ 20 h and then propagate inward at $\sim 90 \mu\text{m/h}$ (Fig. 5B right), similar to the radial velocity fronts in Fig. 2D. A CIP zone also develops at late times between the central and edge zones in small tissues (Fig. 5B left, magenta streak from 16 h onward).

Next, we studied the evolution of the fractions of G1, G2, and post-mitotic cells (SI Materials and Methods) in the boundary and central regions of the tissues. In both small and large tissues, the boundary region is primarily populated by rapidly-cycling cells (Fig. 5C): After about 12 h of tissue expansion, the boundary zone predominantly contains cells that have recently divided (post-mitotic, black) or are likely to divide soon (G2, green). The high numbers of post-mitotic cells

indicate that cells in G1 rapidly proceed to mitosis.

The center of small tissues (Fig. 5D, left) has similar cell-cycling dynamics to the boundary region, except that the fraction of cells in G1 starts to increase slightly at ~ 40 h. Thus, in the large central vortices of small tissues, cells are also rapidly cycling. In sharp contrast, the center zone of large tissues clearly undergoes cell-cycle arrest at about 30 h (Fig. 5D, right). At this time, cells ceased moving from G1 to G2, while cells in G2 or M-phase continued to division and re-entered G1. Before that, the center of large tissues exhibits large-scale coordinated cell cycling dynamics in the form of anti-phase oscillations. Specifically, peaks in G2 fraction were accompanied by troughs in G1 fraction until the onset of cell cycle arrest at 30 h. In addition, a cell division pulse takes place immediately after stencil removal in all tissues, which manifests as a decrease in G2 and increase in post-mitotic fraction (Fig. 5C,D). These short-time features are especially notable because plots reflect averages over several tissues.

Finally, we sought to link cell-cycle dynamics to the kin-

matics of tissue expansion by studying correlations between local measurements of cell cycle, cell speed, and cell density (Fig. 5E). Here, each point represents one PIV pixel, with color indicating its average cell-cycle state. As expected, cell speed is negatively correlated with cell density. Further, in large tissues, the cell-cycle state transitions from G1-dominated to G2-dominated when cell density increases above ~ 5000 cells/mm² and cell speed falls below ~ 12 μ m/h (Fig. 5E right). In this regime, the decrease of cell speed with increasing cell density bears similarities to previously-reported glass transitions and contact-inhibition-of-locomotion (CIL) (39, 42). Small tissues, by contrast, lack the G1-dominated, slow, high-density cell population (Fig. 5E, left) found in the center of large tissues. These plots emphasize the connection between cell-cycling behavior and the mechanical state of a tissue.

Discussion

We began this study with the question of how the size of an epithelium dictates its overall expansion and growth. Our assays systematically dissected this question, from the overall boundary dynamics (Fig. 1) to the internal biophysical dynamics (Figs. 2, 3, 4), and then related these behaviors to the cell-cycle dynamics (Fig. 5). While we ultimately demonstrated that ‘small’ tissues expand proportionally much faster than do ‘large’ tissues, our data point towards a surprising and stark decoupling of the behaviors of the outer and inner regions of an expanding epithelium. Notably, the edge zones of epithelia are largely independent of tissue size and history, while interior dynamics are very much dependent on size and mechanical history.

Unexpectedly, the overall tissue growth and expansion dynamics (Fig. 1) could be attributed to one dominant feature: our epithelia expanded at a constant edge speed (about 30 μ m/hr). Our model for epithelial expansion relied only on this single parameter and accurately predicted expansion in a variety of contexts, proving that the size effects we observed on overall areal expansion rates are driven by the perimeter-to-area ratio of the tissues. To further emphasize the decoupling of the boundary and internal dynamics of epithelia, consider that the key findings in Fig. 1 neither predict nor depend upon the radically different internal dynamics we observed within ‘small’ and ‘large’ tissues. For instance, despite the roiling vortices occupying large portions of ‘small’ tissues and the pronounced, large-scale contact inhibition of ‘large’ tissues—two antithetical phenomena—no hints of these behaviors can be detected in the motion of the boundary, which again depends only on a constant radial expansion speed.

Interestingly, the type and timing of internal dynamics were dependent not only on size but also upon the history of the given tissue. For instance, while a small tissue eventually grows to reach the initial size of a large tissue, it exhibits different internal dynamics from the large tissue at this size. While edge dynamics are stereotyped and conserved across different sizes, tissue size ultimately dictates the evolution of growth patterns within the bulk of the tissue by altering the constraints under which the tissue grows.

The vortices are a striking and unexpected example of such internal dynamics. In particular, our data suggest a strong correlation of vortex formation with the development of non-monotonic density profiles. Not only small tissues exhibited co-occurrence of vortices with density decreases in the tissue center, but also off-center vortices in large tissues were always preceded by a density decrease at the vortex core (SI Appendix, Fig. S5). These findings should help to guide future work probing the mechanistic basis of these tissue vortices to consider density effects.

The pronounced decoupling between boundary and internal dynamics in epithelia confers stability to the overall expansion of the tissue, making it robust to a wide range of internal perturbations. From the perspective of collective behavior, we speculate that such robust boundary dynamics may be beneficial in a tissue whose teleology is to continuously expand to sheath organ surfaces. Further, the ability to accurately predict epithelial expansion with a single parameter will have practical uses in experimental design and tissue-engineering applications. Finally, given that many of the key phenomena presented here only occurred due to the millimetric scale of our unconfined tissues and the long duration of the experiments, our results showcase the value of pushing the boundaries of large-scale, long-term studies on freely-expanding tissues.

All experiments were performed with MDCK-II cells expressing the FUCCI cell-cycle marker system (33) on tissue-culture plastic dishes coated with type-IV collagen (MilliporeSigma, USA). Tissue velocity vector fields were calculated from phase contrast image sequences using the free MATLAB package PIVLab (45). For cell density calculation, we developed and trained a convolutional neural network to reproduce nuclei from 4X phase contrast images and counted the number of nuclei within local windows across the tissue. We also used these nuclei for cell tracking (46) and calculation of local cell cycle fraction. We calculated individual tissue kymographs by averaging together measurements within bins of distance from the tissue’s original center for each timepoint. For average kymographs, we averaged the kymographs of individual tissues, aligning by the center point.

R.A. acknowledges support from the Human Frontiers of Science Program (LT000475/2018-C).

1. Rudolf Ludwig Karl Virchow. Cellular-Pathologie. *Archiv für pathologische Anatomie und Physiologie und für klinische Medizin*, III:3–39, 1855.
2. M. Abercrombie and Joan E.M. M Heaysman. Observations on the social behaviour of cells in tissue culture. II. “Monolayering” of fibroblasts. *Experimental Cell Research*, 6(2): 293–306, 1954. ISSN 00144827. doi: 10.1016/0014-4827(54)90176-7.
3. Peter Friedl and Darren Gilmour. Collective cell migration in morphogenesis, regeneration and cancer. *Nature Reviews Molecular Cell Biology*, 10(7):445–457, 2009. ISSN 14710072. doi: 10.1038/nrm2720.
4. Ricard Alert and Xavier Trepat. Physical Models of Collective Cell Migration. *Annual Review of Condensed Matter Physics*, 11(1):77–101, 2020. ISSN 1947-5454. doi: 10.1146/annurev-conmatphys-031218-013516.
5. Vincent Hakim and Pascal Silberzan. Collective cell migration: A physics perspective. *Reports on Progress in Physics*, 80(7):076601, 2017. ISSN 00344885. doi: 10.1088/1361-6633/aa65ef.
6. Kevin Doxzen, Sri Ram Krishna Vedula, Man Chun Leong, Hiroaki Hirata, Nir S. Gov, Alexandre J. Kabla, Benoit Ladoux, and Chwee Teck Lim. Guidance of collective cell migration by substrate geometry. *Integrative Biology (United Kingdom)*, 5(8):1026–1035, 2013. ISSN 17579708. doi: 10.1039/c3ib40054a.
7. M. Deforet, V. Hakim, H. G. Yevick, G. Duclos, and P. Silberzan. Emergence of collective modes and tri-dimensional structures from epithelial confinement. *Nature Communications*, 5(May):3747, 2014. ISSN 20411723. doi: 10.1038/ncomms4747.

8. Jacob Notbohm, Shiladitya Banerjee, Kazage J.C. C. Uluje, Bomi Gweon, Hwanseok Jang, Yongdo Park, Jennifer Shin, James P. Butler, Jeffrey J. Fredberg, and M. Cristina Marchetti. Cellular Contraction and Polarization Drive Collective Cellular Motion. *Biophysical Journal*, 110(12):2729–2738, 2016. ISSN 15420086. doi: 10.1016/j.bpj.2016.05.019.
9. Carlos Pérez-González, Ricard Alert, Carles Blanch-Mercader, Manuel Gómez-González, Tomasz Kolodziej, Elsa Bazellieres, Jaume Casademunt, and Xavier Trepat. Active wetting of epithelial tissues. *Nature Physics*, 15(1):79–88, 2019. ISSN 17452481. doi: 10.1038/s41567-018-0279-5.
10. Grégoire Peyret, Romain Mueller, Joseph D'Alessandro, Simon Begnaud, Philippe Marcq, René Marc Mège, Julia M. Yeomans, Amin Doostmohammadi, and Benoît Ladoux. Sustained Oscillations of Epithelial Cell Sheets. *Biophysical Journal*, 117(3):464–478, 2019. ISSN 15420086. doi: 10.1016/j.bpj.2019.06.013.
11. Vanni Petrolli, Magali Le Goff, Monika Tadrus, Kirsten Martens, Cédric Allier, Ondrej Mandula, Lionel Hervé, Silke Henkes, Rastko Sknepnek, Thomas Boudou, Giovanni Cappello, and Martial Balland. Confinement-Induced Transition between Wavelike Collective Cell Migration Modes. *Physical Review Letters*, 122(16):168101, 2019. ISSN 10797114. doi: 10.1103/PhysRevLett.122.168101.
12. Thomas Lecuit and Pierre François Lenne. Cell surface mechanics and the control of cell shape, tissue patterns and morphogenesis. *Nature Reviews Molecular Cell Biology*, 8(8):633–644, 2007. ISSN 14710072. doi: 10.1038/nrm2222.
13. M. Pujade, E. Grasland-Mongrain, A. Hertzog, J. Jouanneau, P. Chavrier, B. Ladoux, A. Buguin, and P. Silberzan. Collective migration of an epithelial monolayer in response to a model wound. *Proceedings of the National Academy of Sciences of the United States of America*, 104(41):15988–15993, 2007. ISSN 00278424. doi: 10.1073/pnas.0705062104.
14. Xavier Trepat, Michael R. Wasserman, Thomas E. Angelini, Emil Millet, David A. Weitz, James P. Butler, and Jeffrey J. Fredberg. Physical forces during collective cell migration. *Nature Physics*, 5(6):426–430, 2009. ISSN 17452481. doi: 10.1038/nphys1269.
15. L. Petitjean, M. Refay, E. Grasland-Mongrain, M. Pujade, B. Ladoux, A. Buguin, and P. Silberzan. Velocity fields in a collectively migrating epithelium. *Biophysical Journal*, 98(9):1790–1800, 2010. ISSN 15420086. doi: 10.1016/j.bpj.2010.01.030.
16. M. Refay, L. Petitjean, S. Coscoy, E. Grasland-Mongrain, F. Amblard, A. Buguin, and P. Silberzan. Orientation and polarity in collectively migrating cell structures: Statics and dynamics. *Biophysical Journal*, 100(11):2566–2575, 2011. ISSN 15420086. doi: 10.1016/j.bpj.2011.04.047.
17. Kenekchuku David Nnetu, Melanie Knorr, Dan Strehle, Mareike Zink, and Josef A. Käs. Directed persistent motion maintains sheet integrity during multi-cellular spreading and migration. *Soft Matter*, 8(26):6913–6921, 2012. ISSN 1744683X. doi: 10.1039/c2sm07208d.
18. Xavier Serra-Picamal, Vito Conte, Romaric Vincent, Ester Anon, Dhananjay T Tambe, Elsa Bazellieres, James P. Butler, Jeffrey J. Fredberg, and Xavier Trepat. Mechanical waves during tissue expansion. *Nature Physics*, 8(8):628–634, 2012. ISSN 1745-2473. doi: 10.1038/nphys2355.
19. Min Zhao, Tingrui Pan, Gong Zhang, Jiandong Wu, Alex Mogilner, Zhengping Xu, Simon Liao, Guoqing Xu, Yan Zhang, Francis Lin, Wolfgang Losert, Zijie Zhu, Yohui Sun, and Rachel M. Lee. Collective cell migration has distinct directionality and speed dynamics. *Cellular and Molecular Life Sciences*, 74(20):3841–3850, 2017. ISSN 1420-682X. doi: 10.1007/s00018-017-2537-6.
20. Marina Uroz, Sabrina Wistorf, Xavier Serra-Picamal, Vito Conte, Marta Sales-Pardo, Pere Roca-Cusachs, Roger Guimera, and Xavier Trepat. Regulation of cell cycle progression by cell-cell and cell-matrix forces. *Nature Cell Biology*, 20(6):646–654, 2018. ISSN 14764679. doi: 10.1038/s41556-018-0107-2.
21. Sham Tlili, Estelle Gauquelin, Brigitte Li, Olivier Cardoso, Benoît Ladoux, Héliane Delanoë Ayari, and François Graner. Collective cell migration without proliferation: Density determines cell velocity and wave velocity. *Royal Society Open Science*, 5(5):172421, 2018. ISSN 20545703. doi: 10.1098/rsos.172421.
22. Hwanseok Jang, Jacob Notbohm, Bomi Gweon, Youngbin Cho, Chan Young Park, Sun Ho Kee, Jeffrey J. Fredberg, Jennifer H. Shin, and Yongdo Park. Homogenizing cellular tension by hepatocyte growth factor in expanding epithelial monolayer. *Scientific Reports*, 8(April):45844, 2017. ISSN 20452322. doi: 10.1038/srep45844.
23. Claudio G. Rolli, Hidekazu Nakayama, Kazuo Yamaguchi, Joachim P. Spatz, Ralf Kemmerer, and Jun Nakanishi. Switchable adhesive substrates: Revealing geometry dependence in collective cell behavior. *Biomaterials*, 33(8):2409–2418, 2012. ISSN 01429612. doi: 10.1016/j.biomaterials.2011.12.012.
24. Alberto Puliafito, Lars Hufnagel, Pierre Neveu, Sebastian Streichan, Alex Sigal, D. Kuchnir Fyngson, and Boris I. Shraiman. Collective and single cell behavior in epithelial contact inhibition. *Proceedings of the National Academy of Sciences of the United States of America*, 109(3):739–744, 2012. ISSN 00278424. doi: 10.1073/pnas.1007809109.
25. Rachel M. Lee, Douglas H. Kelley, Kerstin N. Nordstrom, Nicholas T. Ouellette, and Wolfgang Losert. Quantifying stretching and rearrangement in epithelial sheet migration. *New Journal of Physics*, 15(2):025036, 2013. ISSN 13672630. doi: 10.1088/1367-2630/15/2/025036.
26. Grégoire Beaune, Tomita Vasilica Stirbat, Nada Khalifat, Olivier Cochet-Escartin, Simon Garcia, Vasily Valefevitch Gurchenkov, Michael P. Murrell, Sylvie Dufour, Damien Cuvelier, and Françoise Brochard-Wyart. How cells flow in the spreading of cellular aggregates. *Proceedings of the National Academy of Sciences of the United States of America*, 111(22):8055–8060, 2014. ISSN 10916490. doi: 10.1073/pnas.1323788111.
27. Sri Ram Krishna Vedula, Man Chun Leong, Tan Lei Lai, Pascal Hersen, Alexandre J. Kabla, Chwee Teck Lim, and Benoît Ladoux. Emerging modes of collective cell migration induced by geometrical constraints. *Proceedings of the National Academy of Sciences of the United States of America*, 109(32):12974–12979, 2012. ISSN 00278424. doi: 10.1073/pnas.1119313109.
28. Daniel J. Cohen, W. James Nelson, and Michel M. Maharbiz. Galvanotactic control of collective cell migration in epithelial monolayers. *Nature Materials*, 13(4):409–417, 2014. ISSN 14764660. doi: 10.1038/nmat3891.
29. Malcolm S. Steinberg. Differential adhesion in morphogenesis: a modern view. *Current Opinion in Genetics and Development*, 17(4):281–286, 2007. ISSN 0959437X. doi: 10.1016/j.gde.2007.05.002.
30. Christian Dahmann, Andrew C. Oates, and Michael Brand. Boundary formation and maintenance in tissue development. *Nature Reviews Genetics*, 12(1):43–55, 2011. ISSN 14710056. doi: 10.1038/nrg2902.
31. Daniel J. Cohen, Martijn Gloerich, and W. James Nelson. Epithelial self-healing is recapitulated by a 3D biomimetic E-cadherin junction. *Proceedings of the National Academy of Sciences of the United States of America*, 113(51):14698–14703, 2016. ISSN 10916490. doi: 10.1073/pnas.1612208113.
32. Asako Sakaue-Sawano, Hiroshi Kurokawa, Toshifumi Morimura, Aki Hanyu, Hiroshi Hama, Hatsuki Osawa, Saori Kashiwagi, Kiyoko Fukami, Takaki Miyata, Hiroyuki Miyoshi, Takeshi Imamura, Masaharu Ogawa, Hisao Masai, and Atsushi Miyawaki. Visualizing Spatiotemporal Dynamics of Multicellular Cell-Cycle Progression. *Cell*, 132(3):487–498, 2008. ISSN 00928674. doi: 10.1016/j.cell.2007.12.033.
33. S. J. Streichan, C. R. Hoerner, T. Schneidt, D. Holzer, and L. Hufnagel. Spatial constraints control cell proliferation in tissues. *Proceedings of the National Academy of Sciences*, 111(15):5586–5591, 2014. ISSN 0027-8424. doi: 10.1073/pnas.1323016111.
34. Ricard Alert, Carles Blanch-Mercader, and Jaume Casademunt. Active fingering instability in tissue spreading. *Physical Review Letters*, 122(8):088104, 2019. ISSN 10797114. doi: 10.1103/PhysRevLett.122.088104.
35. E. Anon, X. Serra-Picamal, P. Hersen, N. C. Gauthier, M. P. Sheetz, X. Trepat, and B. Ladoux. Cell crawling mediates collective cell migration to close undamaged epithelial gaps. *Proceedings of the National Academy of Sciences*, 109(27):10891–10896, 2012. ISSN 0027-8424. doi: 10.1073/pnas.1117814109.
36. Andrea Ravasio, Ibrahim Cheddadi, Tianchi Chen, Telmo Pereira, Hui Ting Ong, Cristina Bertocchi, Agustí Brugués, Antonio Jacinto, Alexandre J. Kabla, Yusuke Toyama, Xavier Trepat, Nir Gov, Luís Neves De Almeida, and Benoît Ladoux. Gap geometry dictates epithelial closure efficiency. *Nature Communications*, 6(July):7683, 2015. ISSN 20411723. doi: 10.1038/ncomms8683.
37. Thomas E. Angelini, Edouard Hannezo, Xavier Trepat, Jeffrey J. Fredberg, and David A. Weitz. Cell migration driven by cooperative substrate deformation patterns. *Physical Review Letters*, 104(16):168104, 2010. ISSN 00319007. doi: 10.1103/PhysRevLett.104.168104.
38. Kazuhiro Aoki, Yohei Kondo, Honda Naoki, Toru Hiratsuka, Reina E. Itoh, and Michiyuki Matsuda. Propagating Wave of ERK Activation Orients Collective Cell Migration. *Developmental Cell*, 43(3):305–317.e5, 2017. ISSN 18781551. doi: 10.1016/j.devcel.2017.10.016.
39. T. E. Angelini, E. Hannezo, X. Trepat, M. Marquez, J. J. Fredberg, and D. A. Weitz. Glasslike dynamics of collective cell migration. *Proceedings of the National Academy of Sciences*, 108(12):4714–4719, 2011. ISSN 0027-8424. doi: 10.1073/pnas.1010059108.
40. Jin Ah Park, Jae Hun Kim, Dapeng Bi, Jennifer A. Mitchell, Nader Taheri Qazvini, Kelan Tantisira, Chan Young Park, Maureen McGill, Sae Hoon Kim, Bomi Gweon, Jacob Notbohm, Robert Steward, Stephanie Burger, Scott H. Randell, Alvin T. Kho, Dhananjay T. Tambe, Corey Hardin, Stephanie A. Shore, Elliot Israel, David A. Weitz, Daniel J. Tschumperlin, Elizabeth P. Henske, Scott T. Weiss, M. Lisa Manning, James P. Butler, Jeffrey M. Drazen, and Jeffrey J. Fredberg. Unjamming and cell shape in the asthmatic airway epithelium. *Nature Materials*, 14(10):1040–1048, 2015. ISSN 14764660. doi: 10.1038/nmat4357.
41. Dapeng Bi, Xingbo Yang, M. Cristina Marchetti, and M. Lisa Manning. Motility-driven glass and jamming transitions in biological tissues. *Physical Review X*, 6(2):021011, 2016. ISSN 21603308. doi: 10.1103/PhysRevX.6.021011.
42. Juliane Zimmermann, Brian A. Camley, Wouter Jan Rappel, and Herbert Levine. Contact inhibition of locomotion determines cell-cell and cell-substrate forces in tissues. *Proceedings of the National Academy of Sciences of the United States of America*, 113(10):2660–2665, 2016. ISSN 10916490. doi: 10.1073/pnas.1522330113.
43. Zsuzsanna Püspöki, Martin Storath, Daniel Sage, and Michael Unser. Transforms and operators for directional bioimage analysis: a survey. *Focus on Bio-Image Informatics*, pages 69–93, 2016. doi: 10.1007/978-3-319-28549-8.
44. Ricard Alert, Jean-François Joanny, and Jaume Casademunt. Universal scaling of active nematic turbulence. *arXiv*, page 1906.04757, 2019.
45. William Thielicke and Eize Stamhuis. PIVlab-towards user-friendly, affordable and accurate digital particle image velocimetry in MATLAB. *Journal of Open Research Software*, 2(1):e30, 2014. doi: <http://doi.org/10.5334/jors.bl>.
46. Jean Yves Tinevez, Nick Perry, Johannes Schindelin, Genevieve M. Hoopes, Gregory D. Reynolds, Emmanuel Laplantine, Sebastian Y. Bednarek, Spencer L. Shorte, and Kevin W. Eliceiri. TrackMate: An open and extensible platform for single-particle tracking. *Methods*, 115:80–90, 2017. ISSN 10959130. doi: 10.1016/j.ymeth.2016.09.016.